Journal of Alloys and Compounds 509 (2011) 8047–8055

Contents lists available at ScienceDirect

Journal of Alloys and Compounds

journal homepage: www.elsevier.com/locate/jallcom

Effects of non magnetic aluminum Al doping on the structural, magnetic and transport properties in $La_{0.57}Nd_{0.1}Sr_{0.33}MnO_3$ manganite oxide

E. Tka [a], K. Cherif [a], J. Dhahri [a,*], E. Dhahri [b]

[a] Unité de Recherche Physique des Solides, Département de Physique, Faculté des Sciences de Monastir, 5019, Université de Monastir, Tunisia
[b] Laboratoire de Physique Appliqué, Faculté des Sciences, B.P. 1171, 3000 Sfax, Université de Sfax, Tunisia

ARTICLE INFO

Article history:
Received 14 February 2011
Received in revised form 3 May 2011
Accepted 5 May 2011

Keywords:
Manganite
Rietveld refinement
Conduction mechanism
Small polaron hopping (SPH)

ABSTRACT

$La_{0.57}Nd_{0.1}Sr_{0.33}Mn_{1-x}Al_xO_3$ (LNSMAO) compounds were prepared for $x = 0.0$ to 0.3 by solid-state route. The X-ray powder diffraction has shown that all our synthesized samples are a single phase and have crystallized in the hexagonal symmetry with R $\bar{3}$ c space group. It is also worth mentioning that the unit cell volume decreases along with an increasing aluminum (Al) content. The scanning electron microscopy (SEM) has shown smooth and densified structures, clean and pure images. The magnetization and electrical measurements vs. temperature proved that all our samples exhibit a ferromagnetic to paramagnetic transition and a metallic to semiconductor one when the temperature increases. The substitution of Mn by aluminum (Al) leads to a continuous decrease of both the Curie temperature T_C (from 342 K for $x = 0.0$ to 238 K for $x = 0.3$) and the resistivity transition temperature T_P (from 338 K for $x = 0.0$ to 208 K for $x = 0.3$). When analyzing the electrical resistivity data, it has been concluded that the metallic (ferromagnetic) part of the resistivity (ρ) (below T_P) can be explained by the following equation $\rho = \rho_0 + \rho_2 T^2 + \rho_{4.5} T^{4.5}$, signifying the importance of the grain/domain boundary, electron–electron and two magnon scattering processes. However, at a higher temperature ($T > T_P$) the paramagnetic semiconducting regime, the adiabatic small polaron and Variable Range Hopping models are found to fit well.

© 2011 Elsevier B.V. All rights reserved.

1. Introduction

Rare-earth doped manganites of the form $RE_{1-x}A_xMnO_3$ (where RE = La, Nd, Y, Pr. . . and A = Ba, Sr, Ca or Na, K. . .) have been widely investigated due to their remarkable physical and chemical properties, their potential applications in technology, their unusual colossal magnetoresistive (CMR) property as well as their magnetocaloric effect (MCE) [1–4]. The parent compound, $REMnO_3$ is a charge-transfer (CT) insulator with trivalent manganese in different layers coupled among themselves antiferromagnetically through a superexchange mechanism. But within a layer, these Mn^{3+} ions are coupled ferromagnetically. When the RE trivalent element is doped by various elements, a proportionate amount of Mn^{3+} with the electronic configuration ($3d^4$, $t_{2g}^3 \uparrow e_g^1 \uparrow, S = 2$), is replaced by Mn^{4+} with the electronic configuration ($3d^3$, $t_{2g}^3 \uparrow e_g^0, S = 3/2$) creating holes in the e_g band [5]. The holes permit charge transfer in the e_g state which is highly hybridized with the oxygen 2p state. Due to the intra-atomic Hund's rule, this charge transfer induces a ferromagnetic coupling between Mn^{3+} and Mn^{4+} ions which in turn has a dramatic effect on the electrical conductivity [6–9]. This double-exchange (DE) model originally proposed by Zener [10] has been the most prominent underlying physics that describes the simultaneous occurrence of transition from paramagnetic insulator to ferromagnetic metal for most hole-doped manganites. However, with more and more experimental observations, numerous physical mechanisms, including the electron–electron scattering, the small polaron and magnon correlated transport [7,11,12], the lattice distortion effect [13] and the phase-separation-based percolation [12,14], have been proposed to give a more quantitative account on the experimental results obtained from various manganite systems. Nevertheless, there are several ways to change the above-mentioned properties of the manganites. The process reported in the literature most often is the doping of manganites with various elements in two different positions. These are called A-site [15–17] and B-site (or Mn-site) [18–22] substitution. It is believed that the study of the doping effects at the Mn site by other elements with different valences, electron configuration, ionic radius, and non-magnetic ions is very important because of the crucial role of Mn ions in the CMR materials. The Mn-site doping is an effective way to modify the crucial Mn^{3+}–O–Mn^{4+} network [23] and in turn remarkably affects the double exchange effect by modifying the interaction between Mn^{3+}/Mn^{4+} ions via O^{2-} ion network and in turn it largely affects their physical properties as well as CMR. So far, the magnetic ion substitution for the Mn-site and

* Corresponding author. Tel.: +216 73 500278; fax: +216 73 500280.
E-mail addresses: emna_tka@yahoo.fr (E. Tka), cherif_karima@yahoo.fr (K. Cherif), jemai_dhahri@yahoo.fr (J. Dhahri), essebti@yahoo.com (E. Dhahri).

0925-8388/$ – see front matter © 2011 Elsevier B.V. All rights reserved.
doi:10.1016/j.jallcom.2011.05.019

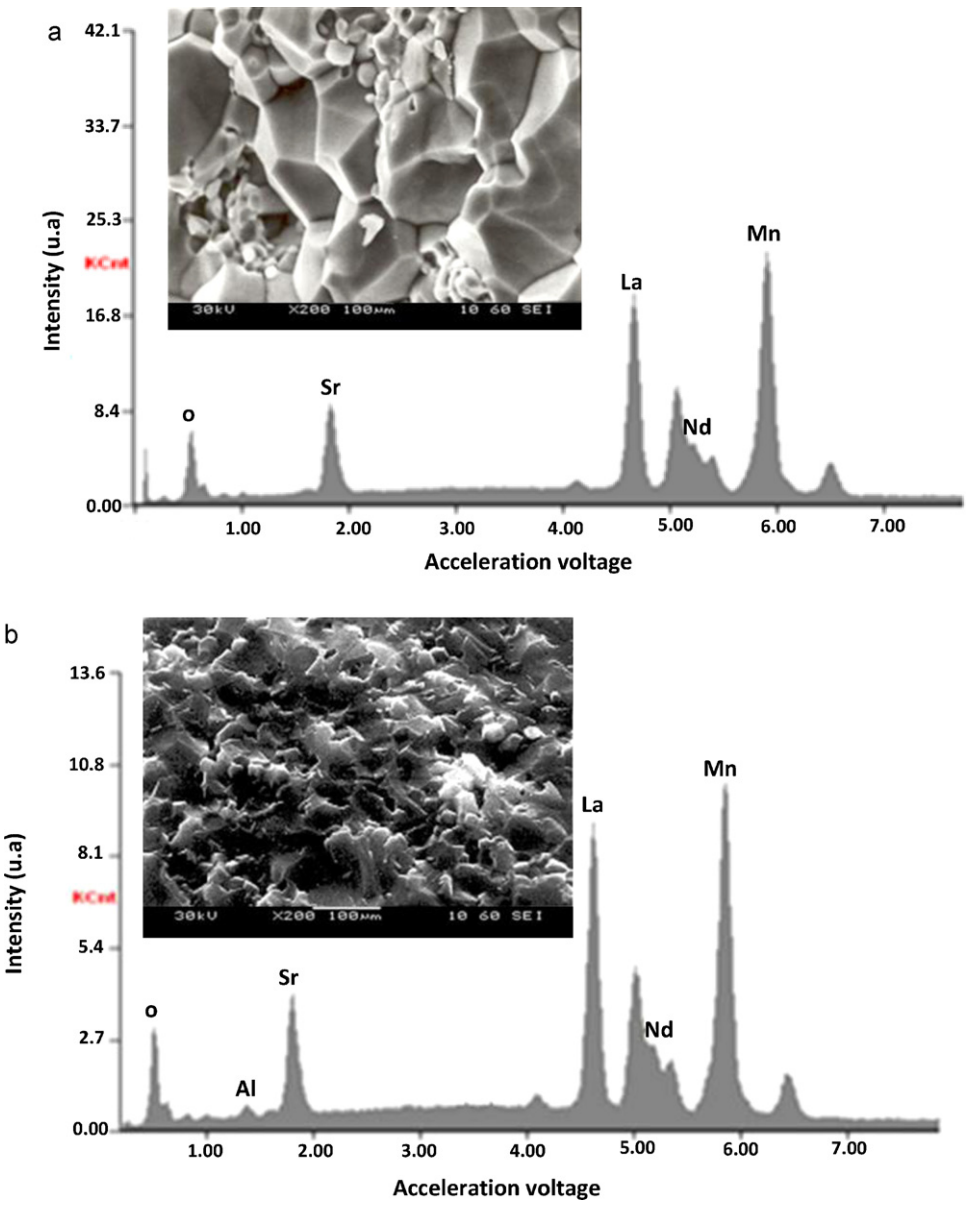

Fig. 1. Plot of EDX analysis of chemical species of $La_{0.57}Nd_{0.1}Sr_{0.33}Mn_{1-x}Al_xO_3$ with (a) $x = 0.0$ and (b) $x = 0.2$. The inset represents the scanning electron micrographs showing the transect surface morphology of pellets prepared in the same condition.

its effect on MR and MC properties have been studied extensively, surprisingly few studies have been carried out on the non-magnetic ion substitution in Mn-sites [24,25]. It is of much interest to know how the presence of a non-magnetic ion in the Mn-site influences the magnetotransport, the MR and MC properties of the material.

In view of these facts, a lot of efforts have been made to obtain information on the effect of Al^{3+} on the structural, magnetic and electrical properties of $La_{0.57}{}^{3+}Nd_{0.1}{}^{3+}Sr_{0.33}{}^{2+}Mn_{0.67-x}{}^{3+}Mn_{0.33}{}^{4+}Al_x{}^{3+}O_3{}^{2-}$ $(0.0 \leq x \leq 0.30)$. The particularity of the Al^{3+} ion is that it is non-magnetic and it has a much smaller ionic radius ($r_{Al^{3+}} = 0.53\,Å$) than that of Mn^{3+} ($r_{Mn^{3+}} = 0.65\,Å$) [26]. An Al doping into Mn sublattice replaces Mn^{3+} by Al^{3+} ([Ne] $3s^2\ 3p^1$) and results in a very small distortion of the crystallographic structure of the polycrystalline compounds (LNSMAO) $(0 \leq x \leq 0.30)$.

2. Experimental details

Polycrystalline samples of (LNSMAO) compounds were prepared by a conventional solid-state reaction method in air. Stoichiometric amounts of La_2O_3, Nd_2O_3, $SrCO_3$, MnO_2 and Al_2O_3 with nominal purities not less than 99.99% have been intimately mixed in an agate mortar in isopropyl alcohol and heated in air at 1173 K for 72 h. After grinding thoroughly, they were pressed into pellet form under $4t/cm^2$ (of about 1 mm thickness) and sintered in air at 1673 K for 24 h with intermediate regrinding and repelleting. Finally, those pellets were quenched to room temperature. This step was carried out in order to keep the structure at annealing temperature. During firing, the pellets were placed on platinum foils.

The phase purity and structure of bulk samples were identified by X-ray diffraction at room temperature using a Siemens D5000 X-ray diffractometer with a graphite monochromatized CuK_α radiation ($\lambda_{CuK_\alpha} = 1.544\,Å$) and $20^\circ \leq 2\theta \leq 120^\circ$ with steps of 0.02° and a counting time of 18 s per step. According to our measurements, this system is able to detect up to a minimum of 3% of impurities.

The structure refinement has been carried out by the Rietveld analysis of the X-ray powder diffraction data with FULLPROF software (version 1.9c-May 2001-LLB-JRC) [27]. A scanning electron microscopy (SEM) equipped with an energy dispersive X-ray system was also used for overall microstructural and compositional analysis. The pictures were taken at room temperature on a Phillips XL30 equipped with a field emission gun at 20 kV.

Magnetization (M) vs. temperature (T) was measured by a Foner magnetometer equipped with a superconducting coil in a magnetic field of 0.05 T.

The resistivity measurements as a function of temperature were carried out by using the four-probe method without applying the magnetic field. The samples were cut into square shapes, with a typical dimension of 1 mm × 80 mm.

Table 1
Results of EDX analysis.

	Typical cationic composition from EDX					Nominal composition
	La	Nd	Sr	Mn	Al	
$x = 0.00$	0.60	0.12	0.36	0.90	–	$La_{0.57}Nd_{0.1}Sr_{0.33}MnO_3$
$x = 0.05$	0.58	0.11	0.34	0.93	0.04	$La_{0.57}Nd_{0.1}Sr_{0.33}Mn_{0.95}Al_{0.05}O_3$
$x = 0.10$	0.57	0.14	0.31	0.87	0.08	$La_{0.57}Nd_{0.1}Sr_{0.33}Mn_{0.90}Al_{0.10}O_3$
$x = 0.15$	0.55	0.11	0.33	0.86	0.14	$La_{0.57}Nd_{0.1}Sr_{0.33}Mn_{0.85}Al_{0.15}O_3$
$x = 0.20$	0.57	0.14	0.31	0.78	0.18	$La_{0.57}Nd_{0.1}Sr_{0.33}Mn_{0.80}Al_{0.20}O_3$
$x = 0.30$	0.56	0.14	0.31	0.69	0.27	$La_{0.57}Nd_{0.1}Sr_{0.33}Mn_{0.70}Al_{0.30}O_3$

3. Results and discussion

3.1. Energy dispersive analysis

In order to check the existence of all the elements in the (LNSMAO) ($0.0 \le x \le 0.30$) compounds energy dispersive X-ray analysis was performed. The EDX spectra represented in Fig. 1 reveals the presence of La, Nd, Sr, Mn and Al, which confirms that there is no loss of any intergrated element during the sintering. The EDX analysis shows that the chemical compositions of these compounds are close to the nominal ones (La:Nd:Sr:Mn:Al = 0.57:0.1:0.33:1−*x*:*x*). The typical cationic composition for the samples is represented in Table 1. These results are very close to the nominal ones within the experimental uncertainties and, since no secondary phases are seen in the XRD patterns, it is reasonable to assume that aluminum (Al) has been substituted for Mn in this sample.

3.2. Scanning electron microscope

Fig. 1a and b shows the morphology and particle size in the secondary electron imaging mode of (LNSMAO) for $x = 0.0$ and 0.2 respectively. These micrographs show that the doping of Al^{3+} has strongly reduces the grain size which decreases from 250 nm for $x = 0$ down to 110 nm for $x = 0.2$. This obviously indicates that the incorporation of aluminum into Mn-sites inhibits the grain growth during the sintering process at 1673 K.

However, we can also calculate the average grain size (G_s) from the XRD peaks using the Scherer formula $G_s = 0.9\lambda/\beta\cos\theta$, where λ is the X-ray wavelength employed, θ is the diffraction angle for the most intense peak ($h\,k\,l \equiv (1\,0\,4)$) for all samples, and β is defined as $\beta^2 = \beta_m^2 - \beta_s^2$. Here, β_m is the experimental full width at half maximum (FWHM) and β_s is the FWHM of a standard silicon sample [28]. The as-obtained G_s are 81 nm and 44 nm for the samples with $x = 0$ and 0.2, respectively. However, the particle sizes observed by SEM are several times larger than those calculated by XRD, which indicates that each particle observed by SEM consists of several crystallized grains.

3.3. Structural properties

All samples (LNSMAO) with ($x = 0.0$, 0.05, 0.1, 0.15, 0.2, 0.3) are in a single phase condition. The diffraction peaks are sharp and can be indexed on a rhombohedra structure for $0.574\,\text{Å} \le \langle r_B \rangle \le 0.610\,\text{Å}$ with the R $\bar{3}$ c space group, hexagonal setting ($z = 6$), in which the La/Nd/Sr atoms are at 6a (0, 0, 1/4), Mn/Al at 6b (0, 0, 0) and O at 18e (x, 0, 1/4) positions. No traces of secondary phases were detected within the sensitivity limits of the experiment (a few percent). The XRD patterns of our synthesized samples have been refined using Rietveld method. The profile refinement is started with scale and background parameters followed by the unit cell parameters. Then, the peak asymmetry and preferred orientation corrections are applied. Finally, the positional parameters and the individual isotropic parameters are refined. We plot in Fig. 2 the X-ray diffraction patterns for $x = 0.2$ including the observed and calculated profiles as well as the difference profile. We notice that the calculated diffraction lines can be attributed to the existence of preferential orientation of the crystallites in the samples. On the basis of refined crystallographic data, the unit cell and atomic parameters and other fitting parameters of all the samples were computed and are given in Table 1. In Table 1, the residuals for the weighted pattern R_{wp}, the pattern R_p, the structure factor R_F and the goodness of fit χ^2 are also reported. Since final R_F of refinements was always less than 4.01% which is comparable with those results found in literature [25]. It is clear from Fig. 3 that unit cell parameters and volume are found to decrease almost linearly with

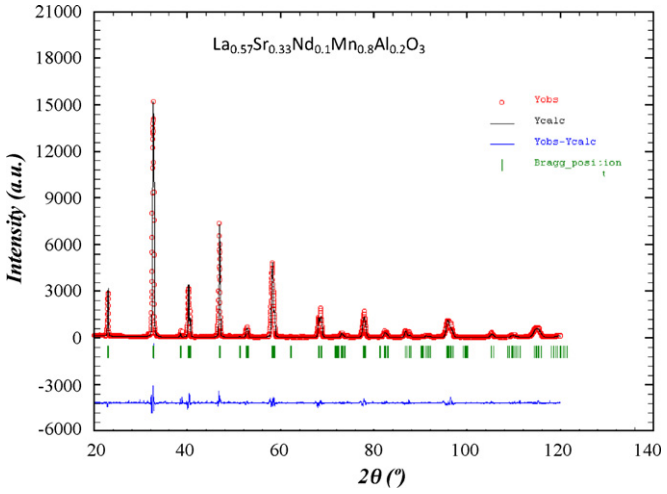

Fig. 2. Observed (open symbols) and calculated (solid lines) X-ray diffraction pattern for $La_{0.57}Nd_{0.1}Sr_{0.33}Mn_{0.80}Al_{0.20}O_3$. Positions for the Bragg reflection are marked by vertical bars. Differences between the observed and the calculated intensities are shown at the bottom of the diagram.

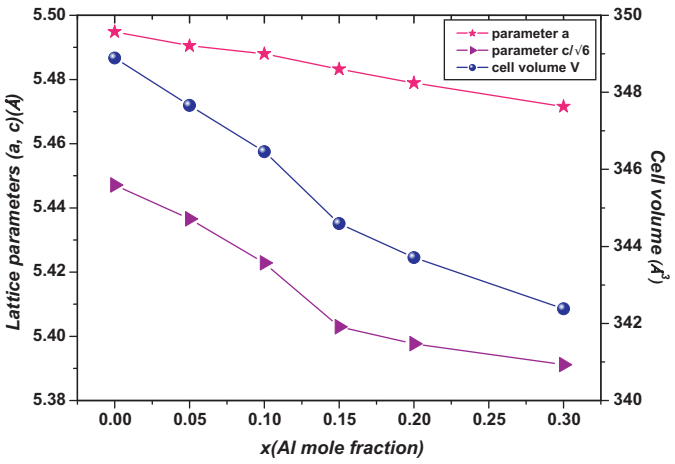

Fig. 3. Variation of lattice parameters and unit cell volume as a function of x for $La_{0.57}Nd_{0.1}Sr_{0.33}Mn_{1-x}Al_xO_3$ ($0.0 \le x \le 0.30$).

Table 2
Crystallographic data of $La_{0.57}Nd_{0.1}Sr_{0.33}Mn_{1-x}Al_xO_3$ manganite system from X-ray diffraction measurements at various Al concentrations (x).

	Sample					
	$x=0.0$	$x=0.05$	$x=0.1$	$x=0.15$	$x=0.2$	$x=0.3$
R $\bar{3}$ c space						
a (Å)	5.4949(8)	5.4905(3)	5.4880(1)	5.4832(2)	5.4789(4)	5.4716(3)
c (Å)	13.3426(2)	13.3169(5)	13.2832(4)	13.2344(1)	13.2216(7)	13.2056(2)
V (Å^3)	348.89(1)	347.66(2)	346.46(6)	344.59(2)	343.71(3)	342.38(7)
(La/Nd/Sr) (6a) B_{iso} (Å^2)	0.62(2)	0.55(3)	0.39(2)	0.48(1)	0.37(4)	0.64(6)
(Mn/Al) (6b) B_{iso} (Å^2)	0.48(2)	0.37(4)	0.25(1)	0.16(1)	0.52(8)	0.40(2)
(O) (18e) B_{iso} (Å^2)	1.29(9)	1.92(4)	1.76(5)	1.32(2)	1.54(7)	1.30(1)
x (O)	0.471(3)	0.465(2)	0.463(1)	0.461(1)	0.458(4)	0.455(3)
Descrepancy factors						
R_F (%)	3.33	2.82	4.01	3.97	2.52	3.73
R_p (%)	7.90	6.68	6.21	5.32	7.10	8.60
R_{wp} (%)	5.94	8.78	9.50	10.10	10.44	7.20
χ^2 (%)	3.91	3.25	2.42	3.64	1.94	1.71

increasing B-site cation radius in the case of rhombohedra symmetry samples.

In order to discuss quantitatively the ion match between A and B site ions in perovskite structure compounds, a geometrical quantity Goldschmidt tolerance factor (t) is usually introduced and t is defined as: $t = (r_A + r_O)/\sqrt{2}(r_B + r_O)$ [29], here r_A, r_B and r_O are the average ionic radius of A, B and oxygen, respectively in the perovskite ABO_3 structure. Oxide based manganite compounds have a perovskite structure if their tolerance factor lies in the limits of $0.75 < t < 1$ and in an ideal case the value must be equal to unity. As the calculated values of t of all the samples of the present investigation are within range (Table 3), one may conclude that they might be having a stable perovskite structure.

What is interesting to note from Table 3 is that t values increase continuously with the increasing ionic radius of B-site. It is logical to conclude that there is an increase in the structural distortion thus an increase in the mean steric distortion factor D with an increasing x (Table 3). The as-defined factor D is: $D = 1/3\sum_i \left|a_i - \bar{a}/a_i\right| \times 100$ where $\bar{a} = (a_1 \quad a_2 \quad a_3)^{1/3}$, $a_1 = a_2 = a$, $a_3 = c/\sqrt{6}$, a and c are the lattice parameters [30]. This distortion does not change the lattice symmetry, but only modifies the cell deformation. The rhombohedra distortion may be viewed as a rotation of the octahedral around the three-fold axis by an angle ω from the ideal perovskite position. This rotation describes the buckling of the MnO_6 octahedra caused by the ionic radii mismatch between A and B cations. The angle of rotation ω may be calculated from the oxygen position using $\omega = \arctan(\sqrt{3} - x\sqrt{12})$ [31]. The values obtained are 5.736, 6.913, 7.303, 7.694, 8.278 and 8.860 for $x = 0.0$, 0.05, 0.10, 0.15, 0.2 and 0.3 respectively, indicating huge distortions of all the compositions. For regular Mn coordination octahedral, the relation between ω and the superexchange (Mn/Al–O–Mn/Al) bond angle is given by $\cos\theta = (1 - 4\cos^2\omega)/3$ [32]. When using the values of ω we have obtained θ in reasonable agreement with that obtained from refinement (Table 3). The departure from 180° of (Mn/Al–O–Mn/Al) bond angle is a measure of the distortion. It is noteworthy that the behaviors of $d_{(Mn/Al)-O}$ and of $\theta_{(Mn/Al)-O-(Mn/Al)}$ have opposite effects on the unit-cell volume, which for a distorted perovskite, can be expressed as [17]; $V = z[2d_{(Mn/Al)-O}\cos\omega)]^3$ where $\omega = [\pi - \theta_{(Mn/Al-O-Mn/Al)}/2]$ and z is the number of formula units in the unit cell ($z = 6$ in the present case). The functional dependence of the volume as a function of the concentration x of Al is reproduced using the observed values of $d_{(Mn/Al)-O}$ and $\theta_{(Mn/Al)-O-(Mn/Al)}$ in the above expression.

3.4. Magnetic properties

The investigation of the magnetic properties measured in a magnetic field of 0.05 T proved that all the samples exhibit a single magnetic transition and behave in a ferromagnetic manner at a low temperature ($T \leq T_C$) and in paramagnetic manner above the Curie temperature T_C ($T \geq T_C$) as shown in Fig. 4. This result confirms well the good quality of our samples. The Curie temperature T_C which is defined as the inflection point of M–T curve is summarized in Table 4 for all the samples. According to Table 4, we can see that T_C decreases gradually with an increasing aluminum (Al) content x. This is in correlation with a decrease in (Mn/Al–O–Mn/Al) bond angle when the $\langle r_B \rangle$ decreases as shown in Fig. 5 where we plotted $\theta_{(Mn/Al)-O-(Mn/Al)}$, T_C as a function of $\langle r_B \rangle$. The key factor for the decrease in T_C value is that entering of the aluminum as Al^{3+} into the samples and taking place of the Mn^{3+} cations can reduce the number of available hopping sites, create cuts in the conduction path, and change the Mn^{3+}/Mn^{4+} ratio. Since the Al^{3+} ion is non-magnetic, there is no exchange interaction between Al^{3+}–O–$Mn^{3+/4+}$. Therefore, the decrease in T_C of the aluminum containing compound can be also attributed to the weak of the DE interaction between Mn^{3+}–O–Mn^{4+} mainly due to the decrease of the number of Mn^{3+} ion. For comparison, the T_C values of $La_{0.7}Sr_{0.33}Mn_{0.9}B_{0.1}O_3$ compounds (B = Al, Cr, Mn, Fe, Co, Ni, Cu and Ga) are illustrated in Fig. 6. Since Al^{3+} and Ga^{3+} are non-magnetic ions, there is no exchange interaction between Al^{3+}–O–$Mn^{3+/4+}$ and Ga^{3+}–O–$Mn^{3+/4+}$. Our results are similar to those of Blasco et al. [24]. The fact that the T_C of the Cr-doped compound is slightly higher than that of Ga and the Al-doped compounds can be ascribed to the existence of the super exchange interaction between Cr^{3+} and $Mn^{3+/4+}$. The effect of Fe^{3+} substitution at the Mn sites on T_C is

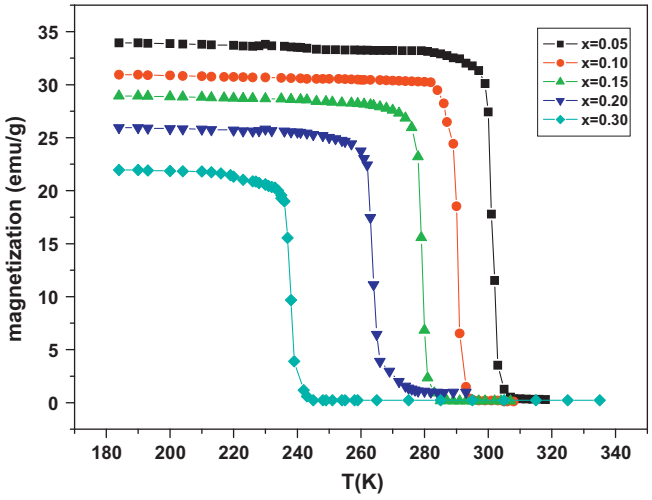

Fig. 4. Magnetization of $La_{0.57}Nd_{0.1}Sr_{0.33}Mn_{1-x}Al_xO_3$ as a function of temperature measured at H = 500 Oe.

Table 3
Values of average distance and angle in $La_{0.57}Nd_{0.1}Sr_{0.33}Mn_{1-x}Al_xO_3$.

	x					
	0.0	0.05	0.1	0.15	0.2	0.3
Structure rhombohedric (R $\bar{3}$ c)						
$d_{(Mn/Al)-O}$ (Å)	1.940(6)	1.944(1)	1.948(1)	1.954(2)	1.962(2)	1.974(1)
$\theta_{(Mn/Al)-O-(Mn/Al)}$ (°)	173.5(1)	169.8(1)	168.7(1)	168.1(1)	167.6(1)	167.2(1)
t	0.975	0.978	0.981	0.984	0.987	0.993
$\langle r_B \rangle$ (Å)	0.610	0.6044	0.5984	0.5924	0.5864	0.5744
D	0.389	0.439	0.532	0.656	0.659	0.665
ω (°)	5.736	6.913	7.303	7.694	8.278	8.860
w (10^{-2})	9.81	9.72	9.64	9.53	9.39	9.19

Table 4
Transition temperature T_C, T_P, Curie Weiss temperature θ_{CW}, experimental μ_{eff}^{cal}, and calculated μ_{eff}^{meas}, effective paramagnetic moments.

Composition	T_C (K)	T_P (K)	ρ_{peak} (Ω cm)	$\mu_{eff}^{cal}(\mu_B)$	$\mu_{eff}^{meas}(\mu_B)$	θ_{CW} (K)	σ^2 (10^{-3} Å^2)
$La_{0.57}Nd_{0.1}Sr_{0.33}MnO_3$	342	328	0.008	4.72	4.66	347	3.183
$La_{0.57}Nd_{0.1}Sr_{0.33}Mn_{0.95}Al_{0.05}O_3$	300	240	0.080	4.59	4.54	302	3.392
$La_{0.57}Nd_{0.1}Sr_{0.33}Mn_{0.90}Al_{0.10}O_3$	289	229	0.101	4.46	4.41	291	3.529
$La_{0.57}Nd_{0.1}Sr_{0.33}Mn_{0.85}Al_{0.15}O_3$	279	216	0.132	4.32	4.26	280	3.560
$La_{0.57}Nd_{0.1}Sr_{0.33}Mn_{0.80}Al_{0.20}O_3$	263	209	0.166	4.18	4.03	268	3.587
$La_{0.57}Nd_{0.1}Sr_{0.33}Mn_{0.70}Al_{0.30}O_3$	238	208	0.208	3.89	3.62	238	3.594

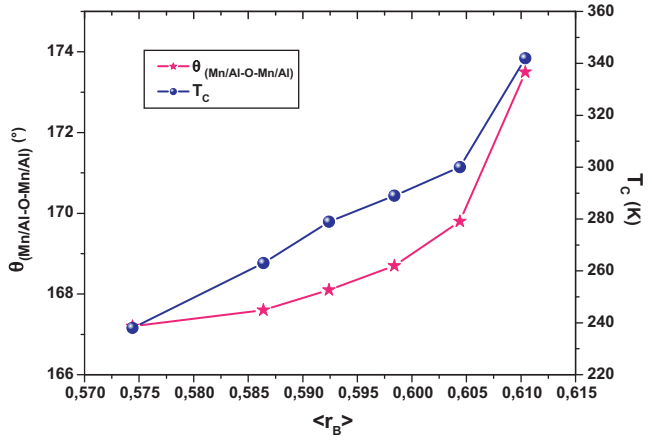

Fig. 5. Variation of bond angle $\theta_{(Mn/Al-O-Mn/Al)}$ and T_C with $\langle r_B \rangle$ for $La_{0.57}Nd_{0.1}Sr_{0.33}Mn_{1-x}Al_xO_3$.

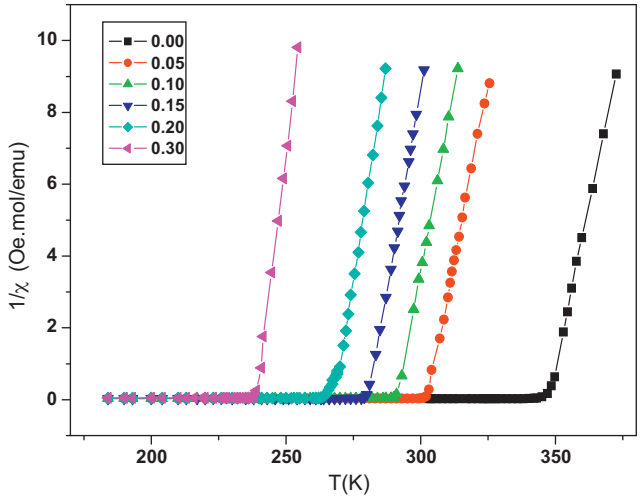

Fig. 7. The temperature dependence of the inverse of the magnetic susceptibility for $La_{0.57}Nd_{0.1}Sr_{0.33}Mn_{1-x}Al_xO_3$ ($0.0 \le x \le 0.30$).

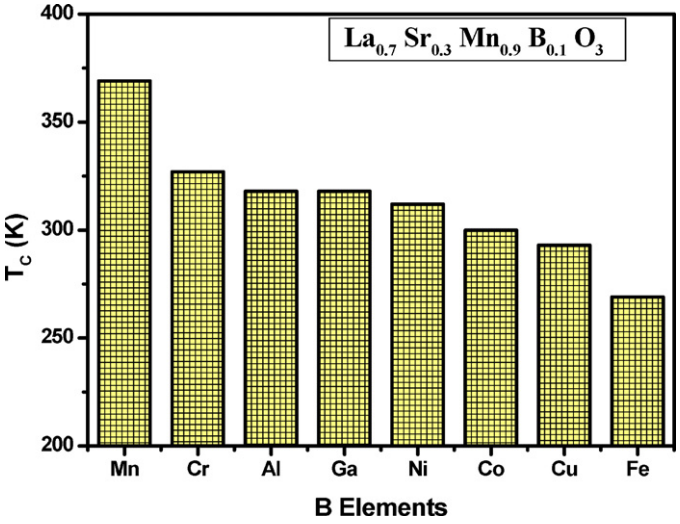

Fig. 6. The Curie temperature (T_C) for $La_{0.7}Sr_{0.3}Mn_{0.9}B_{0.1}O_3$ compounds with B = Mn, Cr, Al, Ga, Ni, Co, Cu, Fe [8,18–22].

most striking among all the B metals. The existence of the Fe^{3+} (e_g^2)–O–Mn^{3+} (e_g^1) super exchange interaction may strongly affect the Mn^{3+}–O–Mn^{4+} DE interaction and could be responsible for the lower T_C value [34]. The magnetic exchange interactions between the B (B = Co, Ni and Cu) [35,36] and Mn ions may also affect the T_C value. The difference in T_C of these compounds is mainly due to the difference in the electronic configuration of the B ions. In fact, the aluminum (Al) substitution in Mn site has been studied by Blasco et al. [24] and Turilli and Licci [37] in $La_{2/3}Ca_{1/3}Mn_{1-x}Al_xO_3$ compounds and they observed a strong suppression of T_C at the rate of $dT_C/dx = 12$ K/Al% However, in large e_g bandwidth CMR materials, such as $La_{1-x}Sr_xMnO_3$ and $La_{1-x}Ba_xMnO_3$, dT_C/dx because of aluminum (Al) doping is reported to be 5–8 K/Al% [38].

Fig. 7 shows the temperature dependence of the inverse magnetic susceptibility χ of all the samples. In the paramagnetic region the susceptibility χ was analyzed by using the Curie Weis law $\chi(T) = H/M = C/(T - \theta_{CW})$ where θ_{CW} is the Curie Weiss temperature which can be determined by the interception of $1/\chi$ curve with the temperature axis and C is the Curie constant defined as: $C = (\mu_0/3k_B)[g^2J(J+1)\mu_B^2] = (\mu_0/3k_B)\mu_{eff}^2$ where $\mu_0 = 4\pi \times 10^{-7}$ H m^{-1} is the permeability, g is the

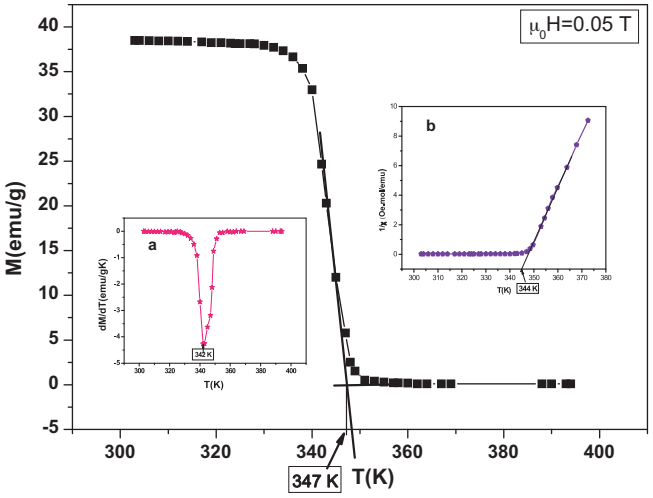

Fig. 8. Temperature dependence of magnetization for the sample with $x = 0.0$ at a magnetic field of 0.05 *T*. The inset a- indicates the plot of dM/dT curve for determining T_C, and the inset b- is the plot of Curie Weiss law vs. temperature.

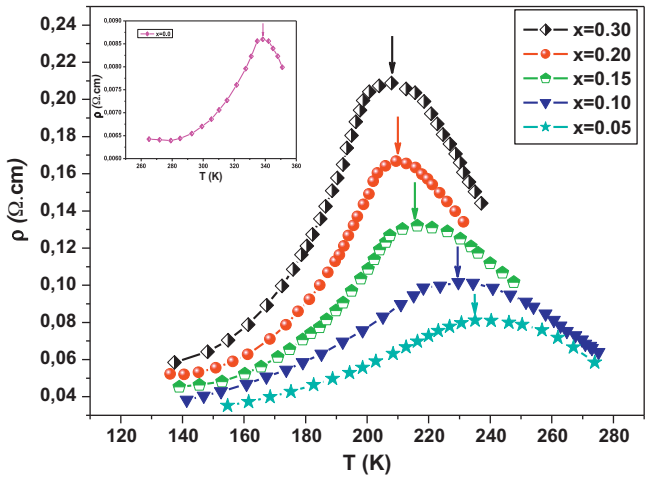

Fig. 9. Temperature dependence of the resistivity ρ (Ω cm) in zero field for $La_{0.57}Nd_{0.1}Sr_{0.33}Mn_{1-x}Al_xO_3$ ($0.05 \le x \le 0.30$). The inset is for ($x = 0.0$).

gyromagnetic ratio, $\mu_B = 9.27 \times 10^{-24}\,JT^{-1}$ is the Bohr magneton, $k_B = 1.38 \times 10^{-23}\,JK^{-1}$ is the Boltzmann constant, $J = L + S$ is the total moment and μ_{eff} is the effective paramagnetic moment. The experimental values (μ_{eff}^{meas}) can be compared to (μ_{eff}^{cal}) the calculated effective paramagnetic moment per formula unit which can be written as: $\mu_{eff}^{cal} = \sqrt{(0.67 - x)[\mu_{eff}^{th}(Mn^{3+})]^2 + 0.33[\mu_{eff}^{th}(Mn^{4+})]^2 + 0.1[\mu_{eff}^{th}(Nd^{3+})]^2}$ with $\mu_{eff}^{th}(Mn^{3+}) = 4.9\,\mu_B$, $\mu_{eff}^{th}(Mn^{4+}) = 3.87\,\mu_B$ and $\mu_{eff}^{th}(Nd^{3+}) = 3.62\,\mu_B$ [39]. (μ_{eff}^{meas}), (μ_{eff}^{cal}) and θ_{CW} are listed in Table 4. As seen in this table θ_{CW} is positive and decreases with x and thus follows the same trend of T_C. The paramagnetic moments (μ_{eff}^{meas}) are close to the calculated values (μ_{eff}^{cal}).

To determine the value of Curie temperature T_C, we have used three methods shown in Fig. 8 which displays the temperature dependence of magnetization of $La_{0.57}Nd_{0.1}Sr_{0.33}MnO_3$ sample.

Method I: A linear extrapolation of M (T) to zero magnetization.
Method II: A determination of inflection point of the transition by using the numerical derivation dM/dT as indicated in the a-inset of Fig. 8.
Method III: A linear fit of the curve $1/\chi$ as a function of T in the paramagnetic region as shown in the b-inset of Fig. 8. The obtained values of T_C are 347 K, 342 K and 344 K, respectively. They are slightly the same. The small difference is mainly due to the observed broad magnetic transition. According to the DE theory [40], there is a stronger overlap between Mn-3d and O-2p orbital results in a larger charge carrier bandwidth W favoring DE ($W\alpha \cos[1/2(\pi - \theta_{(Mn/Al)-O-(Mn/Al)})]/(d_{(Mn/Al)-O})^{3.5}$), (Mn/Al–O) is the bond length and $\theta_{(Mn/Al)-O-(Mn/Al)}$ is the bond angle [33]. Hence an increase in the (Mn/Al–O) bond length will be responsible for a decreasing W and there by T_C. Therefore the structural analysis (Table 2) of this system also supports this decrease in W and a reduction in T_C which is obtained by doping. Again, the (Mn/Al)–O–(Mn/Al) bond angle is the basic structural parameter which controls the charge carrier mobility. Therefore the decrement in the (Mn/Al)–O–(Mn/Al) bond angle with doping will change the charge carrier concentration in the system, and thus hamper the increment in T_C. A similar effect is found in $La_{2/3}Ca_{1/3}MnO_3$ doped with Indium (In) [41] and Co [35]. This evolution may also be explained either in terms of evolution of the average ionic radius of the B-cation site or in terms of the B-cationic disorder mismatch effect which is quantified by a term called the size variance parameter σ^2 expressed by the formula $\sigma^2 = \sum_i y_i r_i^2 - \langle r_B \rangle^2$ where y_i ($\sum_i y_i = 1$) is the fractional occupancy. Rodriguez-Martinez and Attfield [42] found that with an increasing size variance (see Table 4), the Curie temperature falls monotonically with a corresponding fall in the CMR effect. Furthermore, size disorder induces a lattice strain by causing a random displacement of oxygen ions, there by resulting in a distortion of the MnO_6 octahedra and hence the localization of the electrons. As a matter of fact, a large mismatch in the size of B-site cations results in a random arrangement of Mn^{3+} and Mn^{4+} ions, thereby reducing the value of T_C.

3.5. Electrical properties

The temperature dependences at zero-field resistivity (ρ) for the undoped (the inset) and doped (the main panel) (LNSMAO) compounds ($0.0 \le x \le 0.30$) are shown in Fig. 9.

As expected $\rho(T)$ reveal an overall increase of the maximum resistivity ρ_{max} (peak value) and T_P which is indicated by arrows in Fig. 9 decreases to lower a temperature with an increase in the aluminum content x (see Table 4). In a low temperature the ferromagnetic state ($T < T_P$) and the ρ (T) curves of all the compounds exhibit a metallic behavior (i.e. $d\rho/dT > 0$). With rising temperatures, the metal-semiconductor transition is seen at T_P where $d\rho/dT < 0$ for semiconductor behavior. Similar features have been observed in related series such as $La_{2/3}Ca_{1/3}Mn_{1-x}Al_xO_3$ [24]. The observed behavior may be explained as follows. The successive substitution of Al^{3+} at B-site (Mn^{3+}) reduces the value of $\langle r_B \rangle$. Therefore, $\langle r_B \rangle$ becomes too small to fill the space in the cube centers and for this reason, oxygen tends to move towards the centers, reducing the (Mn/Al)–O–(Mn/Al) bond angle. This deviation in $\theta_{(Mn/Al)-O-(Mn/Al)}$ provides a local trap for e_g electrons and possibly causing phase or domain separation. Moreover, the transfer integral b_{ij} of the electron hopping between Mn^{3+} and Mn^{4+} naturally decreases as $\theta_{(Mn/Al)-O-(Mn/Al)}$ becomes smaller than 180°, causing local lattice distortion of the MnO_6 octahedra which in turn influences the double exchange. Consequently, the tendencies of charge localization increase due to the reduction in the carrier mobility and a broader forbidden band near the Fermi level and thus block the electron transport path. As a result, both the values of T_P and T_C are expected to decrease with a decreasing $\langle r_B \rangle$ [43]. It is also worth mentioning that the T_P of all the samples

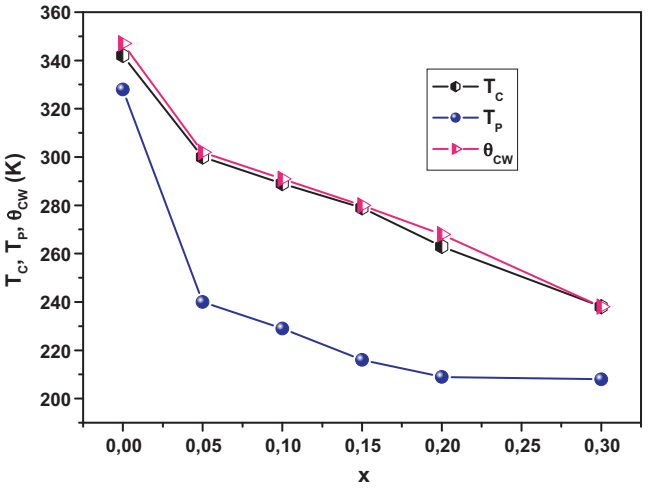

Fig. 10. The relationship between the aluminum composition, x, and the Curie temperature (T_C), the Curie–Weiss temperature (θ_{CW}), the metal-semiconductor transition temperature (T_P) for $La_{0.57}Nd_{0.1}Sr_{0.33}Mn_{1-x}Al_xO_3$ ($0.0 \le x \le 0.30$).

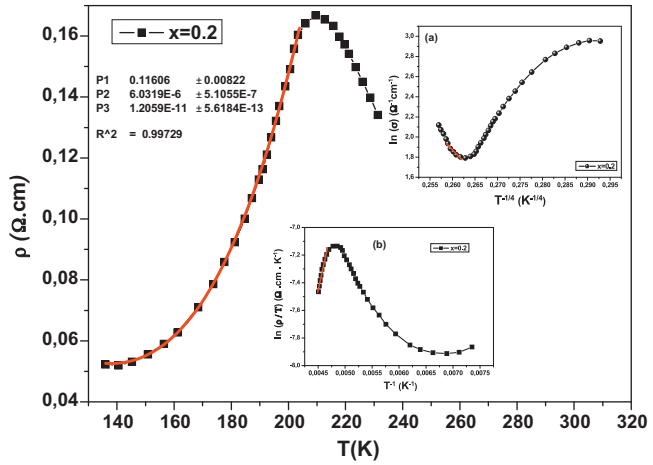

Fig. 11. The main panel represents the plots of the electrical resistivity $\rho(T)$ vs. T for $La_{0.57}Nd_{0.1}Sr_{0.33}Mn_{0.8}Al_{0.2}O_3$. The bold solid line in these plots represents the best fit of experimental data in the metallic regime, below T_P with Eq. (3) $\rho = \rho_0 + \rho_2 T^2 + \rho_{4.5} T^{4.5}$. The (a) inset corresponds to the fit of data in the semiconducting region ($T > T_P$) with equation $\sigma = \sigma_0 \exp(T_0/T)^{1/4}$ below $\theta_D/2$. The (b) inset corresponds to the fit of data with equation $\rho = \rho_\alpha T \exp(E_a/k_B T)$ above $\theta_D/2$. (For interpretation of the references to color in this figure legend, the reader is referred to the web version of this article.)

is lower than their respective T_C. The observed difference can be attributed to the microstructural effect such as oxygen variation or grain boundaries. Similar behavior was previously observed in Al-substituted manganites $Pr_{0.7}(Ca,Sr)_{0.3}Mn_{1-x}Al_xO_3$ [44]. Fig. 10 shows an almost linear decrease in the magnetic transition temperatures T_C, the Curie–Weiss θ_{CW} and the metal-semiconductor transition (T_P) when aluminum content x increases. The T_P temperatures show rather a small divergence of the corresponding T_C. It may be ascribed to the granular character of polycrystalline compounds and the presence of the inter-grain boundaries which dominate the transport properties. Such a phenomenon, which is mainly caused by spins dependent tunneling or scattering processes at the grain boundaries, is called the "extrinsic" MR effect [45].

3.6. Conduction mechanism

3.6.1. Low temperature behavior ($T < T_P$)

In spite of over a decade of intensive work on CMR materials, the variation of resistivity at low temperatures ($T < T_P$) and relative strengths of the different scattering mechanisms originating from different contributions are not yet thoroughly understood. Therefore, an attempt has been made to explain the low temperature regime, where the transport properties fully show the metallic state (below T_P) by fitting with the following three empirical equations [46,47]:

$$\rho = \rho_0 + \rho_2 T^2 \quad (1)$$

$$\rho = \rho_0 + \rho_{2.5} T^{2.5} \quad (2)$$

$$\rho = \rho_0 + \rho_2 T^2 + \rho_{4.5} T^{4.5} \quad (3)$$

In the above equations, ρ_0 in Eq. (1), represents the resistivity due to the grain/domain boundary effects [47,48]. While, $\rho_2 T^2$ in Eqs. (1) and (3) indicates the resistivity due to the electron–electron scattering process [46,49]. $\rho_{2.5} T^{2.5}$ on the other hand is the term arising due to the electron–magnon scattering process in the ferromagnetic phase [47,48,50]. Finally, the term $\rho_{4.5} T^{4.5}$ is a combination of the electron–electron, the electron–magnon and the electron–phonon scattering processes in the ferromagnetic region [49]. Actually, it is assumed that the latter process is more favorable in the half-metallic band structure materials such as manganites.

The experimental data of (LNSMAO) (0.0–0.3) samples fitted the three equations and the quality of this fitting is evaluated by comparing the square of linear correlation coefficient (R^2) obtained for each equation. It is also important to mention that the obtained values of R^2 were as high as 99.9% for Eq. (3) which confirms the applicability of electron–magnon scattering process in the metallic phase. The fitted data are shown by red solid lines in the main panel of Fig. 11 for $La_{0.57}Nd_{0.1}Sr_{0.33}Mn_{0.8}Al_{0.2}O_3$. The best fitted parameters are shown in Table 5. It is noted that the values of ρ_0, ρ_2 and $\rho_{4.5}$ increase with the increase of x. However, the decrease in temperature independent ρ_0 is more significant with x compared to that of ρ_2. Also as the concentration x increases, the size of the domain boundary decreases and ρ_0 becomes larger. In fact, the increment of ρ_2 and $\rho_{4.5}$ with x is due to the suppression of spin fluctuation. Hence, the bandwidth becomes smaller. It can therefore, be concluded that the strength of the electron–magnon scattering term depends not only on the grain growth, but also on how the grain growth has been achieved. These values are comparable to those reported in mixed valent manganites [51].

3.6.2. High temperature behavior ($T > T_P$)

According to the work done by Khiem et al. [52], the electrical resistivity just above T_P is explained by Variable Range Hopping (VRH) model, while Small Polaron Hopping (SPH) model which is considered at temperatures beyond $\theta_D/2$ (θ_D, is the Debye's temperature which is estimated from the plots of $\ln(\rho/T)$ vs. $1/T$ (b-inset of Fig. 11) by taking the deviation from linearity as equal to $\theta_D/2$). In the latter case, if the activated energies for hopping to neighboring atoms are not the same, then it may be that hopping to a non-nearest neighbor has a smaller activation energy. This is particularly true at low temperatures [53]. This Variable Range Hopping is more complicated to describe [54] but it can be summarized by Mott's [55] equation: $\sigma = \sigma_0 \exp(-T_0/T)^{1/4}$, where T_0 is the characteristic temperature which is related to the density of states in the vicinity of the Fermi energy $N(E_F)$ by $16\alpha^3/k_B N(E_F)$ where α is the inverse of the localization length, k_B the Boltzmann's constant and $N(E_F)$ is the density of states at the Fermi level, which can be calculated from the slope of the plot of $\ln\sigma$ vs. $T^{-1/4}$ curves (a-inset of Fig. 11) with using the value of $\alpha = 2.22\ \mathrm{nm}^{-1}$ calculated by Viret et al. [56]. One drawback of (VRH) models is that the values of T_0 are often implausibly high ($\sim 10^6$ K) [57] which result an increase in bending of Mn–O–Mn bond and hence it reflects the enhancement

Table 5
The best fit parameters obtained from the experimental resistivity data for the metallic behavior (below T_P) and for semiconductor behavior (above T_P) for $La_{0.57}Nd_{0.1}Sr_{0.33}Mn_{1-x}Al_xO_3$ ($x = 0.0$–0.2) compounds.

Sample code	$\rho = \rho_0 + \rho_2 T^2 + \rho_{4.5} T^{4.5}$				$\alpha = \alpha_0 \exp(-T_0/T)^{1/4}$			$\rho = \rho_\alpha T \exp(E_a/k_B T)$			
	ρ_0 (Ω cm)	ρ_2 (Ω cm K^{-2})	$\rho_{4.5}$ (Ω cm K$^{-4.5}$)	R^2	T_0 ($\times 10^6$ K)	$N(E_F)$ (e V^{-1} cm^{-3})	R^2	θ_D (K)	ν_{ph} ($\times 10^{12}$ Hz)	E_a (MeV)	R^2
$x = 0.00$	0.014	1.91×10^{-7}	6.76×10^{-14}	0.999	0.06	3.08×10^{-22}	0.973	–	–	–	–
$x = 0.05$	0.020	2.54×10^{-7}	1.14×10^{-14}	0.999	0.17	1.16×10^{-22}	0.987	606	12.6	62	0.990
$x = 0.10$	0.021	4.01×10^{-7}	1.72×10^{-12}	0.999	1.26	1.60×10^{-21}	0.995	588	12.2	101	0.993
$x = 0.15$	0.077	3.32×10^{-6}	7.23×10^{-12}	0.998	2.19	9.24×10^{-20}	0.988	503	10.4	113	0.987
$x = 0.20$	0.116	6.03×10^{-6}	1.20×10^{-11}	0.997	4.96	4.09×10^{-20}	0.969	471	9.8	136	0.976
$x = 0.30$	0.142	8.21×10^{-6}	1.73×10^{-11}	0.999	8.85	2.29×10^{-20}	0.995	466	9.7	230	0.967

of carrier effective mass or a narrowing of the bandwidth which in turn results in drastic change in the resistivity. In fact, it sharpens and sharpening the resistivity peak in the vicinity of T_P [58]. These Values are in perfect agreement with the previously reported values [59]. The estimated values of T_0 and $N(E_F)$ are given in Table 5. It is noticed that the values are increasing continuously with the application of the concentration of Al, however, $N(E_F)$ values are found to be decreasing due to the decrease in the DE interaction. N_{ph} (the optical phonon frequencies) were obtained from the relation of ($h\nu_{ph} = k_B\theta_D$). The values of phonon frequency and $\theta_D/2$ decreased against aluminum concentration. This indicates that the frequency of lattice wave decreases when there is an increase in the Nd content. It seems that the values of $\theta_D/2$ are much higher than T_P, which highlights the width of VRH region between $\theta_D/2$ and T_P.

The conduction mechanism of manganites at high temperatures, $T > \theta_D/2$ is governed by thermally activated small polarons. In this model, the lattice distortions are of a size similar to that of the unit cell and the polarons move between the nearest neighbor sites. The resistivity in this case is expressed by:

$$\rho = \rho_\alpha T \exp\left(\frac{E_a}{k_B T}\right) \quad \text{(adiabatic)}.$$

However, the strong electron–polaron coupling means that the motion of charge-carriers is slow compared with the lattice vibration. The motion of the electrons and the lattice cannot be separated, and the analysis in a non-adiabatic limit is more complicated [54] and the resistivity is given by:

$$\rho = \rho_\alpha T^{3/2} \exp\left(\frac{E_a}{k_B T}\right) \quad \text{(non-adiabatic)}.$$

where E_a is the activation energy and ρ_α is the residual resistivity and is given by: $\rho_\alpha = 2k_B/3ne^2a^2\nu$, k_B here is the Boltzmann's constant, e is the electronic charge, n is the number of density of charge carriers, a is the site-to-site hopping distance, and ν is the longitudinal optical phonon frequency. Following the work done by Jung [60], the adiabatic small polaron-hopping model is used in the current investigation.

The activation energy values calculated in the best-fit parameters are described in Table 5 and the corresponding plot is shown in b-inset of Fig. 11 for $x = 0.2$. It is clear from table that, the activation energy (E_a) values are increasing with the increase in Al content. The observed behavior reflects the increase in polaron more clearly than Mn ions in the lattice.

4. Conclusions

$La_{0.57}Nd_{0.1}Sr_{0.33}Mn_{1-x}Al_xO_3$ powder samples have been synthesized by using the standard ceramic process for the composition range $0.0 \le x \le 0.3$. We have investigated their structural, magnetic and transport properties. The result of the Rietveld refinement of X-ray powder diffraction shows that these compounds crystallize in the rhombohedral structure with R $\bar{3}$ c space group with increasing aluminum content for $0.574\,\text{Å} \le \langle r_B \rangle \le 0.610\,\text{Å}$. While, the unit cell volume decreases due to the replacement of larger Mn^{3+} ions by smaller Al^{3+} ions. The magnetic measurement shows that all samples undergo a single paramagnetic ferromagnetic transition and the Curie temperature decreases with increasing Al-doping content. This effect can be explained by a weakening of the ferromagnetic double exchange interaction. The electrical studies of this manganese perovskite show that the value of the resistance increases whereas T_P decreases when the level of aluminum (Al) increases. The resistivity dependence on temperature shows a transition from metal to semiconductor phase. It has also been concluded that the electrical conduction mechanism in the metallic regime at low temperatures ($T < T_P$) can be explained on the basis of grain boundary effects and the single electron–magnon scattering process. Resistivity data were well fitted with the relation $\rho = \rho_0 + \rho_2 T^2 + \rho_{4.5} T^{4.5}$, whereas the adiabatic Small Polaron Hopping (SPH) mechanism and Variable Range Hopping mechanism (VRH) can be used in the high temperature ($T > T_P$).

References

[1] M. Dominiczak, A. Ruyter, P. Limelette, I. Monot-Laffez, F. Giovannelli, M.D. Rossell, G. Van Tendeloo, Solid State Commun. 148 (2008) 340–344.
[2] B.P. McCarthy, L.R. Pederson, Y.S. Chou, X.-D. Zhou, W.A. Surdoval, L.C. Wilson, J. Power Sources 180 (2008) 294–300.
[3] L. Millar, H. Taherparvar, N. Filkin, P. Slater, J. Yeomans, Solid State Ionics 179 (2008) 732–739.
[4] N. Dhahri, A. Dhahri, K. Cherif, J. Dhahri, H. Belmabrouk, E. Dhahri, J. Alloys Compd. 507 (2010) 405–409.
[5] K. Cherif, J. Dhahri, E. Dhahri, M. Oumezzine, H. Vincent, J. Solid State Chem. 163 (2002) 466–471.
[6] S.K. Misra, S.I. Andronenko, S. Asthana, D. Bahadur, J. Magn. Magn. Mater. 322 (2010) 2902–2907.
[7] S.S. Ata-Allah, M.F. Mostafa, Z. Heiba, H.S. Refai, Physica B 406 (2011) 801–811.
[8] Z. Xinghua, L. Zhiqing, J. Rare Earth 29 (2011) 230–234.
[9] L. Joshi, S. Keshri, Measurement 44 (2011) 938–945.
[10] C. Zener, Phys. Rev. 81 (1951) 440.
[11] N. Ibrahim, A.K. Yahya, S.S. Rajput, S. Keshri, M.K. Talari, J. Magn. Magn. Mater. 323 (2011) 2179–2185.
[12] H.D. Varshney, D. Choudhary, M.W. Shaikh, E. Khan, Eur. Phys. J. B 76 (2010) 327–338.
[13] J. Burgy, A. Moreo, E. Dagotto, Phys. Rev. B 71 (2005) 184425–184431.
[14] V.S. Zakhvalinskii, R. Laiho, A.V. Lashkul, K.G. Lisunov, E. Lähderanta, Yu.S. Nekrasova, P.A. Petrenko, P.A. Stamov, J. Phys.: Condens. Matter 23 (2011) 015802–015810.
[15] Y. Kalyana Lakshmi, P. Venugopal Reddy, J. Alloys Compd. 470 (2009) 67–74.
[16] P.K. Siwach, P. Srivastava, H.K. Singh, A. Asthana, Y. Matsui, T. Shripathi, O.N. Srivastava, J. Magn. Magn. Mater. 321 (2009) 1814–1820.
[17] A. Tozri, E. Dhahri, E.K. Hlil, Phys. Lett. A 375 (2011) 1528–1533.
[18] N. Dhahri, A. Dhahri, K. Cherif, J. Dhahri, K. Taibi, E. Dhahri, J. Alloys Compd. 496 (2010) 69–74.
[19] M.T. Tlili, M. Bejar, E. Dhahri, M. Sajieddine, M.A. Valente, E.K. Hlil, Mater. Charact. 62 (2011) 243–247.
[20] S. Mollah, I. Dhiman, A. Das, Mater. Lett. 65 (2011) 922–925.
[21] A.K. Pramanik, A. Banerjee, Phys. Rev. B 81 (2010) 024431–024436.
[22] Y. Ying, T.W. Eom, N.V. Dai, Y.P. Lee, J. Magn. Magn. Mater. 323 (2011) 94–100.
[23] J.L. García-Muñoz, C. Frontera, P. Beran, N. Bellido, J. Hernández-Velasco, C. Ritter, Phys. Rev. B 81 (2010) 014409–014420.
[24] J. Blasco, J. Garcia, J.M. De Teresa, M.R. Ibarra, J. Perez, P.A. Algarabel, C. Marquin, C. Ritter, Phys. Rev. B 55 (1997) 8905–8910.
[25] J. Dhahri, A. Dhahri, M. Oumezzine, E. Dhahri, J. Magn. Magn. Mater. 320 (2008) 2613–2617.
[26] R.D. Shannon, C.T. Prewitt, Acta Crystallogr. B 25 (1969) 925–946.
[27] H.M. Rietveld, J. Appl. Crystallogr. 2 (1969) 65–71.
[28] A. Guinier, Théorie et Technique de la Radiocristallographie, third ed., Dunod, Paris, 1964, p. 462.

[29] G.H. Jonker, J.H. Van Santen, Physica 16 (1950) 337–349.
[30] Y. Moritomo, A. Asamitsu, Y. Tokura, Phys. Rev. B 51 (1995) 16491–16494.
[31] E. Rodriguez, I. Alvarez, M.L. Lopez, M.L. Veiga, C. Pico, J. Solid State Chem. 148 (1999) 479–486.
[32] M. O'Keeffe, B.G. Hyde, Acta Crystallogr. B 33 (1977) 3802–3813.
[33] P.G. Radaelli, G. Iannone, M. Marezio, H.Y. Hwang, S.W. Cheong, J.D. Jorgensen, D.N. Argyriou, Phys. Rev. B 56 (1997) 8265–8276.
[34] M. Rubinstein, D.J. Gillespie, J.E. Snyder, T.M. Tritt, Phys. Rev. B 56 (1997) 5412–5423.
[35] N. Gayathri, A.K. Raychaudhuri, S.K. Tiwary, R. Gundakaram, A. Arulraj, C.N.R. Rao, Phys. Rev. B 56 (1997) 1345–1353.
[36] I.O. Troyanchuk, D.D. Khalyavin, E.F. Shapovalova, N.V. Kasper, S.A. Guretskii, Phys. Rev. B 58 (1998) 2422–2425.
[37] G. Turilli, F. Licci, Phys. Rev. B 54 (1996) 13052–13057.
[38] I.O. Troyanchuk, M.V. Bushynski, N.V. Pushkarev, H. Szymczak, K. Bärner, J. Magn. Magn. Mater. 225 (2001) 331–336.
[39] C. Kittel, Introduction to Solid State Physics, 6th edition, Wiley, Newyork, 1986, pp. 404–406.
[40] C. Zener, Phys. Rev. 82 (1951) 403–405.
[41] M.C. Sanchez, J. Blasco, J. Stankiewicz, J.M. De Teresa, M.R. Ibarra, J. Solid State Chem. 138 (1998) 226–231.
[42] L.M. Rodriguez-Martinez, J.P. Attfield, Phys. Rev. B 63 (2001) 024424–024428.
[43] S. Bhattacharya, R.K. Mukherjee, B.K. Chaudhuri, H.D. Yang, Appl. Phys. Lett. 82 (2003) 4101–4103.
[44] F. Damay, A. Maignan, N. Nguyen, B. Raveau, J. Solid State Chem. 124 (1996) 385–387.
[45] N. Zhang, W. Ding, W. Zhong, D. Xing, Y. Du, Phys. Rev. B 56 (1997) 8138–8142.
[46] A. Banerjee, S. Pal, B.K. Chaudhuri, J. Chem. Phys. 115 (2001) 1550–1559.
[47] G.J. Snyder, R. Hiskes, S. DiCarolis, M.R. Beasley, T.H. Geballe, Phys. Rev. B 53 (1996) 14434–14444.
[48] J.M. De Teresa, M.R. Ibarra, J. Blasco, J. Garcia, C. Marquina, P.A. Algarabel, Z. Arnold, K. Kamenev, C. Ritter, R. Von Helmolt, Phys. Rev. B 54 (1996) 1187–1193.
[49] A. Urushibara, Y. Morimoto, T. Arima, Phys. Rev. B 51 (1995) 14103–14109.
[50] L. Pi, L. Zheng, Y. Zhang, Phys. Rev. B 61 (2000) 8917–8921.
[51] M. Kar, S. Ravi, Mater. Sci. Eng. B 110 (2004) 46–51.
[52] N.V. Khiem, L.V. Bau, L.H. Son, N.X. Phuc, D.N.H. Nam, J. Magn. Magn. Mater. 262 (2003) 490–495.
[53] N.F. Mott, J. Non-Cryst. Solids 1 (1968) 1–17.
[54] N.F. Mott, E.A. Davis, Electronic Processes in Non-crystalline Materials, Clarendon Press, Oxford, 1970.
[55] N.F. Mott, Metal-Insulator Transitions, Taylor & Francis, London, 1990.
[56] M. Viret, L. Ranno, J.M.D. Coey, Phys. Rev. B 55 (1997) 8067–8070.
[57] J.C. Loudon, PhD Thesis. University of Cambridge (2003).
[58] J. Fontcuberta, B. Martínez, A. Seffar, S. Piñol, J.L. García-Muñoz, X. Obradors, Phys. Rev. Lett. 76 (1996) 1122–1125.
[59] S. Bhattacharya, A. Banerjee, S. Pal, P. Chaudhuri, J. Phys.: Condens. Matter 14 (2002) 10221–10235.
[60] W.H. Jung, J. Mater. Sci. Lett. 17 (1998) 1317–1319.